J. Fluid Mech. (2022), *vol*. 942, A22, doi:10.1017/jfm.2022.382

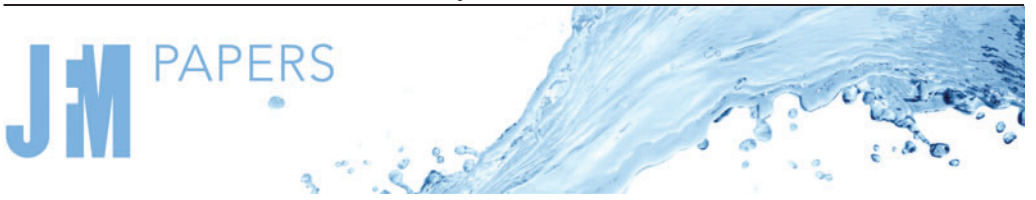

Wake transitions and steady z-instability of an Ahmed body in varying flow conditions

Yajun Fan[1],†, **Vladimir Parezanović**[2] **and Olivier Cadot**[1]

[1]School of Engineering, University of Liverpool, Liverpool L69 3GH, UK

[2]Aerospace Engineering Department, Khalifa University of Science and Technology, Abu Dhabi, UAE

(Received 4 November 2021; revised 7 April 2022; accepted 24 April 2022)

The paper investigates experimentally the flow past a flat-back, taller than wide Ahmed body having rectangular base aspect ratio $H/W = 1.11$ in the context of ground vehicle aerodynamics. Parametric studies at Reynolds number 2.1×10^5 explore the sensitivity of the aerodynamic force and body pressure distribution with respect to varying flow conditions defined from variable ground clearance C (taken at mid-distance from the front and rear axles of the body), pitch angle α, and yaw angle β (equivalent to a crosswind). Two-dimensional parametric maps in the parametric spaces (β, C) and (β, α) are obtained for parameter ranges covering real road vehicle driving conditions. The study of the base pressure gradient reveals non-trivial and sharp transitions identified as significant changes of near wake orientation in both parametric spaces. All unsteady transitions correspond to fluctuation crises of the vertical gradient component only. These transitions are summarized in phase diagram representations. Both phase diagrams in (β, C) and (β, α) parametric spaces can be unified at large yaw in the (β, C_r) space, where the rear clearance C_r separating the lower edge of the base from the ground is a simple function of the pitch α and the clearance C. The impacts of the wake transitions are clearly identified in the base drag, drag, lift and side force coefficients. The contribution of the steady near wake z-instability (Grandemange *et al.*, *Phys. Fluids*, vol. 25, 2013*a*, pp. 95–103) is assessed by repeating the sensitivity analysis with a rear cavity. As reported previously, the rear cavity suppresses the steady instability by symmetrizing the wake. A domain for the existence of the instability is finally proposed in the attitudes map (β, α) defined from regions where the mean lateral force coefficients are significantly decreased by the presence of the rear cavity. In addition, it is found that the steady instability forces the wake to be less unsteady for all attitudes that do not correspond to unsteady transitions.

Key words: shear-flow instability, wakes, bifurcation

† Email address for correspondence: Yajun.Fan@liverpool.ac.uk

1. Introduction

In the industrial context of energy conservation and emission reduction, the aerodynamics of ground vehicles has raised a lot of concern from engineers and researchers. In particular, aerodynamic drag, which is dominant for high-speed driving conditions and proportional to the square of the velocity (Hucho 1998), is now considered as a priority target by car manufacturers to reduce fuel consumption. Thus more research is devoted to aerodynamic drag reduction, together with specific attention paid to the presence of crosswinds, a very common feature for real driving conditions. Howell (2015) investigated different vehicle types, and established that at 10° yaw (producing a crosswind of 17 % of the car speed), the drag coefficient increase is in the range 0.03–0.06 for real car geometries, corresponding to 10–20 % of the drag coefficient at null-yaw condition. As also reported by Howell (2015), this increase is related to an induced drag effect associated with the aerodynamic force component perpendicular to the wind axis. It should be also considered that the vehicle clearance (distance to the ground) and pitch resulting from different mass loading are other flow conditions that also influence the drag.

Most of the fundamental research on ground vehicles aerodynamics focuses on simplified three-dimensional (3-D) bluff bodies, such as the Ahmed body (Ahmed, Ramm & Faitin 1984). In particular, the square-back version of the Ahmed body represents those types of ground vehicles with a flat back, such as minivans, sport utility vehicles, vans or lorries for which the main source of aerodynamic drag is the base pressure, accounting for about 70 % of the total drag (Ahmed *et al.* 1984; Hucho & Sovran 1993). Therefore, research works concentrate on the turbulent recirculating region or near wake aft the body base. For a square-back bluff body (Ahmed or similar bodies), three types of global dynamics have been identified experimentally (Duell & George 1999; Khalighi, Chen & Laccarino 2012; Grandemange, Gohlke & Cadot 2013*b*; Volpe, Devinant & Kourta 2015; Perry, Pavia & Passmore 2016; Evrard *et al.* 2017; Pavia, Passmore & Sardu 2018; Schmidt *et al.* 2018; Haffner *et al.* 2020; Pavia *et al.* 2020) and retrieved numerically (Östh *et al.* 2014; Pasquetti & Peres 2015; Evstafyeva, Morgans & Dalla Longa 2017; Lucas *et al.* 2017; Dalla Longa, Evstafyeva & Morgans 2019; Fan *et al.* 2020; Podvin *et al.* 2020), namely the vortex shedding modes, the pumping motion of the recirculating region and the steady wake instability. While vortex shedding (Roshko 1993) and wake pumping (Berger, Scholz & Schumm 1990) were already recognized as major ingredients of bluff body wake dynamics, the steady instability leading to a permanent wake asymmetry was observed only recently in the seminal work of Grandemange *et al.* (2013*b*). In a crosswind, the flow gets more complex with the creation of 3-D separations along the longitudinal edges of the body, producing a system of streamwise vortices upstream of the recirculating region at the base (Hassaan, Badlani & Nazarinia 2018; McArthur *et al.* 2018). These vortices are associated with induced drag and interact with the recirculating region.

When the body is aligned with the wind axis, the steady instability manifests as left/right (resp. top/bottom) asymmetric mirror states of the near wake aft the base, called y-instability (resp. z-instability). In this terminology, y and z refer to the wake asymmetry directions, where the z-direction is taken perpendicular to the ground. Grandemange, Gohlke & Cadot (2013*a*) showed how the asymmetry direction depends on the base aspect ratio. The y-instability, which is prone to occur for a square back of base aspect ratio $H/W < 1$, corresponds to a pure reflectional symmetry breaking, whereas the z-instability obtained with $H/W > 1$ does not, strictly speaking, because the symmetry in that direction is already broken by the ground and the body supports. Nevertheless, the y- and z-instability origins are the same, and the asymmetry direction corresponds to the

major axis of the rectangular base when the two reflectional symmetries of the geometry are respected (Legeai & Cadot 2020).

The steady instability is sensitive to the distance to the ground (clearance) as well as both the yaw and pitch angles of the model. Grandemange *et al.* (2013*a*) showed that ground clearances larger than 8 % of the body width are necessary to observe the steady instability. The dependency of this critical clearance with the Reynolds number has been studied in Cadot, Evrard & Pastur (2015). For the wake subjected to the y-instability, yaw angles as small as $\beta \approx 1^\circ$ are sufficient to select one of the two mirror asymmetric states involved in the bi-stable dynamics observed at zero yaw (Cadot *et al.* 2015; Volpe *et al.* 2015; Brackston *et al.* 2016; Perry *et al.* 2016; Bonnavion & Cadot 2018). Similarly, the ground, the body supports, the pitch and also the yaw are able to select either bi-stable dynamics or a single state in the case of the z-instability (Bonnavion & Cadot 2018; Bonnavion *et al.* 2019).

Free stream turbulent intensity is also an important factor for ground vehicles aerodynamics as it may reach up to 16 % in real driving conditions (Wordley & Saunders 2008). Turbulent intensity has been investigated recently by Cadot *et al.* (2020) and Burton *et al.* (2021) for an Ahmed body subjected to the y-instability. It is found that the turbulent intensity magnitude does not affect the steady instability strength, and increases the switching rate of the mirror states in the bi-stable dynamics for values larger than 5 %.

Many experiments with either passive or active, open- and closed-loop control noted that cases with a symmetrized wake were often associated with the lowest drag (Grandemange, Gohlke & Cadot 2014; Brackston *et al.* 2016; Evrard *et al.* 2016; Li *et al.* 2016; García de la Cruz, Oxlade & Morrison 2017; Li *et al.* 2019; Lorite-Dıez *et al.* 2020*a*; Urquhart *et al.* 2020, 2021; Haffner *et al.* 2021). However, although Hsu *et al.* (2021) suppressed the wake asymmetry totally using a base suction technique, they found a significant drag increase. This was a consequence of the drastic reduction of the recirculation length with base suction. Actually, the drag varies inversely with this length, as shown by Lorite-Díez *et al.* (2020*b*) using a base blowing technique, which is a feature common to two-dimensional bluff bodies (Bearman 1967) with the condition that the separation on the afterbody remains unaffected. Low drag configurations thus require a long and symmetric recirculating region that is likely achieved using a rear cavity, as shown by Evrard *et al.* (2016) and Lucas *et al.* (2017).

Grandemange *et al.* (2014) and Haffner *et al.* (2020) estimated the drag contribution of the steady instability at between 4 % and 9 % of the total pressure drag. Grandemange *et al.* (2014) interpreted this contribution as an induced drag effect related to the additional cross-flow body force introduced by the steady instability, and Haffner *et al.* (2020) proposed a physical mechanism linking the wake asymmetry to the base suction. The numerical simulation of Podvin *et al.* (2020) confirmed that during the dynamics, increases in the base suction were found to correspond to an increase of the wake asymmetry, along with a shrinkage of the recirculation zone associated with wake pumping.

Large effects of the steady wake instability on the lateral force, i.e. lift or side force coefficient, have been reported during bi-stable dynamics. The wake subjected to the y-instability produces an increase of 0.02 on the side force coefficient (Perry *et al.* 2016; Bonnavion & Cadot 2018; Fan *et al.* 2020), and a similar value for the lift coefficient is found for the z-instability (Bonnavion & Cadot 2018; Bonnavion *et al.* 2019).

Most of the fundamental research cited above has focused on the y-instability, and only Grandemange *et al.* (2013*a*), Bonnavion & Cadot (2018), Castelain *et al.* (2018) and Schmidt *et al.* (2018) reported studies about the z-instability. It has to be acknowledged that real ground vehicles with a square back, such as vans or lorries, are subjected to

the z-instability (Bonnavion *et al.* 2017, 2019). To address fundamentally ground vehicle aerodynamics in variable flow conditions, it is then relevant to study a simplified model subjected to the z-instability. In that context, Bonnavion & Cadot (2018) investigated variation of the flow conditions (clearance, pitch and yaw) for a z-unstable body. Their result indicated that the probability of each flow state is sensitive to the geometrical environment of the recirculating region, such as the ground proximity, the body supports and the body inclination. However, they considered separately the effects of three flow parameters (yaw, clearance and pitch) in inclination ranges of only a few degrees. The present work extends this study to simultaneous yaw and pitch variations likely to happen in real driving conditions.

The fundamental questions to be addressed are twofold: how does the wake evolve when both pitch and yaw are at play, and what is the corresponding wake effect on the aerodynamic performance of the body? These questions are investigated with specific attention to the steady instability in order to assess its impact over a real driving envelope. To the authors' knowledge, there are no results in the literature for systematic and simultaneous variations of pitch, yaw and ground clearance. The experiment first explores the sensitivity of the wake properties measured through the base pressure gradient (Grandemange *et al.* 2013*b*) to the body attitude, and second evaluates the wake contribution to the aerodynamic force (drag, lift and side force components). The paper does not investigate specifically the 3-D separations along the longitudinal edges (McArthur *et al.* 2018) that would require additional measurements. However, their effects are integrated naturally in the measured base suction and the force coefficients.

The paper is organized as follows. The experimental set-up and measurement techniques are described in § 2. In particular, § 2.4 gives the detail concerning the method of the parametric space studies. Results and discussions in § 3 are divided into seven parts. The first part, in § 3.1, focuses on the mean pressure distribution around the body for different attitudes of clearance, yaw and pitch. Then the leeward separation and the wake transitions in two parametric spaces of attitude configurations are investigated in §§ 3.2 and 3.3, respectively. The transitions leading to a fluctuation crisis of the wake are characterized further in § 3.4. The variations of the aerodynamic force components and the link with the wake transitions are studied in § 3.5. Experiments are repeated with a rear cavity in § 3.6, and the wake contribution to the aerodynamics is eventually assessed in § 3.7. Section 4 concludes and offers perspectives on future research.

2. Experimental set-up

2.1. *Model geometry and wind tunnel*

The geometry considered in this work is a square-back Ahmed model (see figures 1*a*,*b*) with dimensions $L = 560$ mm, $W = 180$ mm and $H = 200$ mm. The body is supported by four cylinders of 15 mm diameter, leaving a clearance that can be adjustable from 2 mm to 35 mm. The radius of the rounding of the forebody is 70 mm. The rectangular base in figure 1(*c*) is taller than wide, with aspect ratio $H/W = 1.11$. Two interchangeable afterbodies are used with exactly the same external dimensions – a flat-back version and a rear cavity. The cavity is produced by pushing the rectangular base inwards the body, to create a depth $d = 70$ mm $= 0.35H$, with four sides of thickness $e = 5$ mm. The depth has been chosen to suppress the steady instability, as recommended in Evrard *et al.* (2016) and Lucas *et al.* (2017).

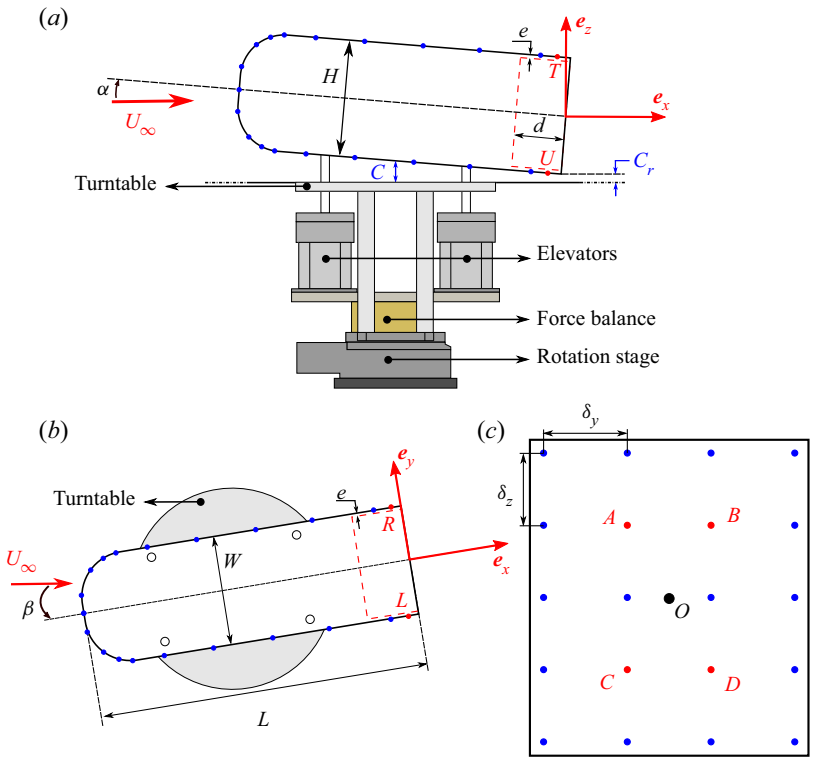

Figure 1. The experimental apparatus and the square-back Ahmed model with the optional rear cavity of depth d represented by the red dashed line: (a) side view, (b) top view, and (c) rear view. The blue and red points mark the pressure taps, where four (T, U, R, L) in (a,b) are used to compute the rear sides pressure gradient $\boldsymbol{j}$, and four (A, B, C, D) in (c) are used for calculating the base pressure gradient $\boldsymbol{g}$.

The model is placed on two Standa 8MVT100-25-1 motorized elevators, to control independently the clearances of the front and rear axles with precision 1 μm. Thanks to this system of two degrees of freedom, the clearance C measured at mid-distance between front and rear axles, and the pitch angle α, can be set independently (see figure 1a). This assembly is mounted on a turntable driven by a motorized rotation stage (Standa 8MR190-90-59) to control the yaw angle β with precision 0.02°. The value $\beta = 0°$ corresponds to a zero side force in the baseline configuration ($C = 20$ mm and $\alpha = 0°$).

The local coordinate system ($\boldsymbol{e}_x, \boldsymbol{e}_y, \boldsymbol{e}_z$) shown in figures 1($a$,$b$) rotates with the turntable: the z-direction is normal to the ground, the y-direction is normal to the lateral sides of the body, and the x-direction completes the direct trihedral; the origin is set at the centre of the body base. It is worth mentioning that the x-direction corresponds to that of the body velocity in the equivalent road testing with crosswind. Nose-up attitude (figure 1a) corresponds to positive pitch angles. We define the ground clearance at the base lower edge as C_r, as shown in figure 1(a).

Experiments are carried out in a blowing wind tunnel having test section 1.2 m wide by 0.6 m high and 2.4 m long. The free stream turbulent intensity is 1 %, and the blockage ratio is 4.9 %. When the body is not in the test section, the ground boundary layer thickness based on 99 % of the free stream velocity is $\delta_{0.99} = 9$ mm at the location of the front of the body. Reference pressure and dynamic pressure q_∞ in the test section are measured with a Furness Control FCO560 precision manometer. In the following, the dynamic pressure

of the uniform flow is set to $q_\infty = 150$ Pa, corresponding to wind speed $U_\infty = 16$ m s^{-1} and Reynolds number $Re = U_\infty H/\nu \approx 2.1 \times 10^5$.

The height of the body H and the free stream velocity U_∞ are chosen as length and velocity scaling units, respectively. For the remainder of this paper, any quantity such as a^* with an asterisk represents those non-dimensional units. For example, the non-dimensional time is defined as $t^* = (tU_\infty)/H$, and the non-dimensional ground clearance is $C^* = C/H$.

2.2. *Force measurements*

The six-component force balance (F/T Sensor: Gamma IP65, manufactured by ATI Industrial Automation) is supporting the two elevators and rotates with the rotary stage as shown in figure 1(*a*). It measures the three components f_x, f_y, f_z in the coordinate system $(\boldsymbol{e}_x, \boldsymbol{e}_y, \boldsymbol{e}_z)$ of figure 1. Time series of the components are acquired at sample frequency 1 kHz. The model frontal area $S = H \times W$ is used to calculate the force coefficients

$$c_i = \frac{f_i}{q_\infty S} \quad (i = x, y, z). \tag{2.1}$$

The force balance resolution is 0.025 N for f_x, f_y, and 0.05 N for f_z, which translates to 5×10^{-3} for c_x, c_y, and 10×10^{-3} for c_z. The force coefficient c_x is related directly to the mechanical power necessary to maintain the velocity V of the body ($V = U_\infty \cos\beta \approx U_\infty$) in the equivalent road condition with crosswind $U_{wind} = U_\infty \sin\beta$. The lowest eigenfrequency of the full mechanical system made of the elevators and the model fixed on the force balance is 9 Hz, corresponding to $f_0^* = 0.11$ in non-dimensional units. No attempts have been made to extract aerodynamic force fluctuation with such a low frequency response of the force balance, and only mean force will be shown. The unsteady aerodynamics will be assessed with pressure measurements that are appropriate.

2.3. *Pressure measurements*

The pressure is measured at 61 locations, as shown in figure 1. There are 20 pressure taps equally spaced at the base with distances $\delta y = 53.3$ mm and $\delta z = 45$ mm (figure 1*c*). There are 41 pressure taps on the four sides and the forebody in the vertical and horizontal middle planes of the geometry. The pressure is measured with a Scanivalve ZOC33/64PX pressure scanner placed inside the body. Tubes connecting taps and scanner never exceed 50 cm, leading to a natural low pass filtering having cut-off frequency approximately 50 Hz. The pressure data are low pass filtered with a moving window of duration 50 ms equivalent to $t_w^* = 3.95$, corresponding to cut-off frequency $f_c = 20$ Hz, i.e. $f_c^* = 0.25$. The sampling frequency is 1 kHz per channel. The static pressure p_∞ of the test section is used to compute the instantaneous pressure coefficient:

$$c_p = \frac{p - p_\infty}{q_\infty}. \tag{2.2}$$

The base suction coefficient c_b is computed from the spatial average of the $N = 20$ pressure taps at the base:

$$c_b = -\frac{1}{N}\sum_{i=1}^{N} c_{pi}. \tag{2.3}$$

The base suction coefficient is always positive and follows trends similar to those for the force coefficient c_x of the model (Roshko 1993).

The pressure scanner accuracy is reported to ± 3.75 Pa by the manufacturer as 0.15 % of the full scale 2.5 kPa. To improve this value, the pressure scanner is calibrated before each measurement in the range ± 200 Pa. The calibration is made using a calibrator and precision manometer (Furness Control FCO650) having accuracy 0.1 % of the reading pressure when larger than 1 Pa. The pressure scanner accuracy is estimated from the measurement of 40 Pa delivered by the calibrator, which is the typical value of the base suction in this present study. All the 64 mean pressures, computed over 10 s with sampling frequency 1 kHz, fall within the range 40 ± 0.5 Pa. We thus estimate this accuracy in term of pressure or base suction coefficients to ± 0.005.

The pressure gradient has been shown in previous research (Grandemange *et al.* 2013*b*; Bonnavion & Cadot 2018) to be an appropriate indicator for the wake asymmetry. Following the same method as Bonnavion & Cadot (2018), the four pressure taps (A, B, C, D) indicated in red in figure 1(c) are used to compute the base pressure gradient components:

$$\left.\begin{aligned} g_y &= \frac{(c_p(B) + c_p(D)) - (c_p(A) + c_p(C))}{2\delta y^*}, \\ g_z &= \frac{(c_p(A) + c_p(B)) - (c_p(C) + c_p(D))}{4\delta z^*}. \end{aligned}\right\} \tag{2.4}$$

In order to assess the rear cavity effect on the wake asymmetry, we use the four pressure taps (T, U, L, R) indicated in red in figures 1(a,b) to compute the rear sides pressure gradient components:

$$\left.\begin{aligned} j_y &= \frac{c_p(R) - c_p(L)}{W^*}, \\ j_z &= c_p(T) - c_p(U). \end{aligned}\right\} \tag{2.5}$$

The advantage of using $\boldsymbol{j}$ instead of $\boldsymbol{g}$ is that the gradient is measured at exactly the same location whether a rear cavity is present or not, thus making the comparison straightforward. In addition, the rear sides are capturing the wake effect that affects the lateral force whose components are the lift and the side force.

All gradient components are low pass filtered with moving window $t_w^* = 3.95$, implying that the dynamics is resolved at low frequencies such that $f^* < 0.25$.

2.4. *Parametric studies*

We investigate the flow properties for different attitudes defined by a given clearance, yaw and pitch. The attitudes are explored in two different two-dimensional parametric spaces. Variations of clearance and yaw correspond to the parametric space (β, C^*, α_0), and variations of pitch and yaw correspond to the space (β, C_0^*, α), where the fixed values are $\alpha_0 = 0^\circ$, and $C_0^* = 0.1$ and 0.125. The values of C_0^* belong to the range of typical ground clearances of passenger cars. Two values are tested to assess the role of the pitch at a given mid-axles clearance.

Parametric spaces are explored with resolution $\delta\beta = 0.5^\circ$, $\delta C^* = 2.5 \times 10^{-3}$ and $\delta\alpha = 0.1^\circ$ within the ranges $\beta \in [-15.5^\circ, 2^\circ]$, $C^* \in [0.01, 0.17]$ and $\alpha \in [-2.3^\circ, 2.3^\circ]$ (resp. $\alpha \in [-3.3^\circ, 3.3^\circ]$) when the clearance is fixed to $C_0^* = 0.1$ (resp. $C_0^* = 0.125$). In total, 2340 attitudes are investigated in the parametric space $(\beta, C^*, \alpha_0 = 0^\circ)$, 1692 in $(\beta, C_0^* = 0.1, \alpha)$, and 2412 in $(\beta, C_0^* = 0.125, \alpha)$.

For each attitude, measurements of force and pressure are performed during a 10 s acquisition. This duration has been chosen as a compromise of the shortest duration to obtain satisfactorily converged averages. The convergences of the mean force components

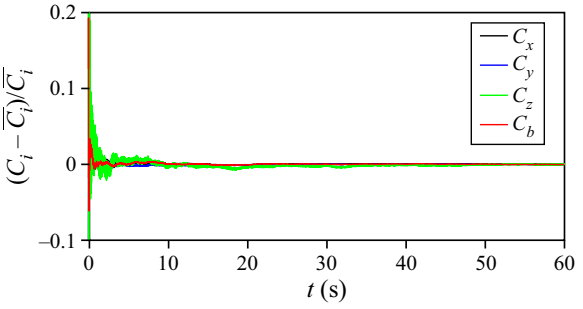

Figure 2. Convergence of the average coefficients of the force components and base suction at the reference attitude.

and base suction coefficients denoted C_i ($i = x, y, z, b$) are shown in figure 2 for the body at the reference attitude ($C^*_{ref} = 0.1, \alpha_{ref} = 0^\circ, \beta_{ref} = -4^\circ$). Full convergences denoted $\bar{C}_i = C_i(T = 60\ \text{s})$ are assumed to be obtained after 60 s, where

$$C_i(T) = \frac{1}{T}\int_0^T c_i(t)\,\mathrm{d}t. \tag{2.6}$$

Figure 2 attests that all values are converged with an accuracy better than 0.5 %. The lift coefficient is observed to have a slower convergence due to its lower resolution (see § 2.3). The completion of all the configurations in a parametric space takes several hours. However, we limit the number of configurations in a run to never exceed a total duration 3.5 hours, which means that all the sensitivity maps presented in the paper are made from two runs. During each run, the temperature increases from 22 °C to 24 °C, and no correction has been applied. Such a long duration raises the issue of signal drifting since both the force balance and the pressure scanner are based on strain gauges technology. The solution is to update regularly the reference of all signals. The update time is estimated from the force balance that suffers from the most significant drift. It is obtained when the amplitude of the drift becomes larger than the high-frequency noise amplitude. This characteristic drift time is 200 s for the force balance. The reference of all signals is obtained from an acquisition of 20 s at the reference attitude chosen for its weak unsteadiness (say $C^*_{ref} = 0.1, \alpha_{ref} = 0^\circ, \beta_{ref} = -4^\circ$).

Practically, when the wind tunnel flow stabilizes after the start, the model is set to the ($C_{ref}, \alpha_{ref}, \beta_{ref}$) reference attitude to take the temporal means of all signals: $\boldsymbol{S_{ref}}$. Then $\boldsymbol{S_{ref}}$ is subtracted from the measurements of the 20 subsequent attitudes, each having a 10 s acquisition time. An update of the reference $\boldsymbol{S_{ref}}$ is then made by resetting the model to the reference attitude. At the end of the parametric exploration, we obtain the total variation of the acquired data from the reference attitude, say $\boldsymbol{s}(t) - \boldsymbol{S_{ref}}$. However, the error made on the force balance measurements is due not only to drift, but also to modifications in the mass distribution (affecting the gravity loading) and to cable deformations by changing the body attitude. In order to remove these non-aerodynamic forces, the parametric exploration is repeated identically as described above but with the wind tunnel switched off ($U_\infty = 0$). For the (β, C^*, α_0) plane exploration, the extreme corrections in absolute value are respectively 9×10^{-3}, 5×10^{-3} and 25×10^{-3} for drag, side force and lift coefficients. For the (β, C^*_0, α) plane exploration, the extreme corrections in absolute value are respectively 6×10^{-3}, 4×10^{-3} and 10×10^{-3} for drag, side force and lift coefficients. The main contribution to these corrections is due to the

vertical axis of the force balance that is not perfectly aligned with the gravity vector. The data are then subtracted from those obtained with the wind. Eventually, the aerodynamic data for the reference attitude S_{ref} are obtained from a separate experiment where the wind data are subtracted from the no-wind data.

3. Results and discussions

As a reminder, H and U_∞ are chosen as length and velocity scaling units, respectively, and any quantity a^* with an asterisk represents those non-dimensional units. We also use the following notation rule: a variable is denoted with a lowercase letter (e.g. $a(t)$), and temporal average is denoted with a uppercase letter, such that the mean is $A = \bar{a}$ and its fluctuation is $A' = \sqrt{\overline{(a-\bar{a})^2}}$.

In § 3.1, we first give an overview of the mean pressure distribution around the body for different attitudes of clearance, yaw and pitch. These illustrations are meant to show the main effect induced by a change of attitude and will be helpful to support the parametric maps involving simultaneous variation of yaw and clearance or pitch shown in the following subsections. The pressure distributions are used in § 3.2 to identify the attitudes having massive leeward separation. Wake transitions are then evidenced in § 3.3, leading to distinctive regions in the parametric spaces. The most unsteady transitions are characterized in § 3.4. The effects of the wake transitions on the force coefficient components are studied in § 3.5. The rear cavity case is examined in § 3.6, and the aerodynamic contribution of the steady instability is assessed in § 3.7.

3.1. *Pressure distribution*

Figures 3–6 show the mean pressure distribution (red arrows and red dashed lines) at the two sections around the body. The grey dashed line in all these figures corresponds to the baseline attitude where $\beta = \alpha = 0^\circ$ and $C^* = 0.1$.

When the ground clearance C^* is increased in figure 3, with the body aligned with the incoming flow ($\beta = \alpha = 0^\circ$), only small changes are observed in the horizontal section (top row). The slight observable increase of the negative pressure on both sides of the forebody indicates a global velocity decrease when the clearance is increased. This is the consequence of the emergence of a flow in the clearance, as shown by the large variation of the pressure distribution in the vertical section (bottom row). In figure 3(*a*, bottom), the lower part of the nose is at $C_p \approx 1$, indicating a high pressure separated region at the front of the body. It is a situation similar to that of the upstream separation of a wall-mounted obstacle (Dargahi 1989). When the body is raised from the ground, the front separation is removed, leading to the emergent underbody flow in figure 3(*b*, bottom). From measurements of Cadot *et al.* (2015), the underbody flow velocity reaches a value close to $0.75U_\infty$ for $C^* = 0.04$ at $Re = 1.5 \times 10^5$. The fluctuating pressure displayed with the magenta line is noticeably important at the forebody wherever the magnitude of the mean pressure is large. For these locations, the value $C_p'/C_p \approx 2\,\%$ is consistent with the wind tunnel free stream turbulent intensity 1 % estimated using the Bernoulli relationship. It seems that there is no noticeable front separation that can be detected. However, the presence of a separation could be missed by the poor spatial resolution of the current pressure measurements, as front separation is often reported for an Ahmed body (Grandemange *et al.* 2013*b*; Fan *et al.* 2020). At the rear, the pressure fluctuation is higher due to the massive separation and can reach 10 % of the mean pressure level, as can be seen in figure 3(*c*).

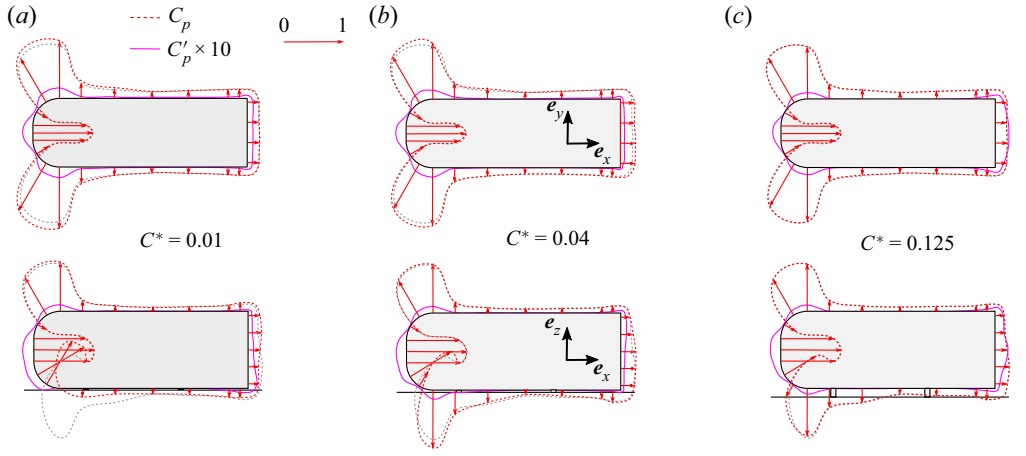

Figure 3. Mean (C_p) and fluctuating (C'_p) pressure coefficient distributions around the horizontal (top row) and vertical (bottom row) central sections of the body. The local pressure C_p is represented by red arrows, negative when pointed outwards from the body surface; C'_p is shown as the magenta continuous line. The grey dashed line is the C_p distribution at the baseline attitude $\beta = \alpha = 0^\circ$ and $C^* = 0.1$. The three cases (*a–c*) depict variations with different ground clearances and body aligned with the incoming flow ($\beta = \alpha = 0^\circ$).

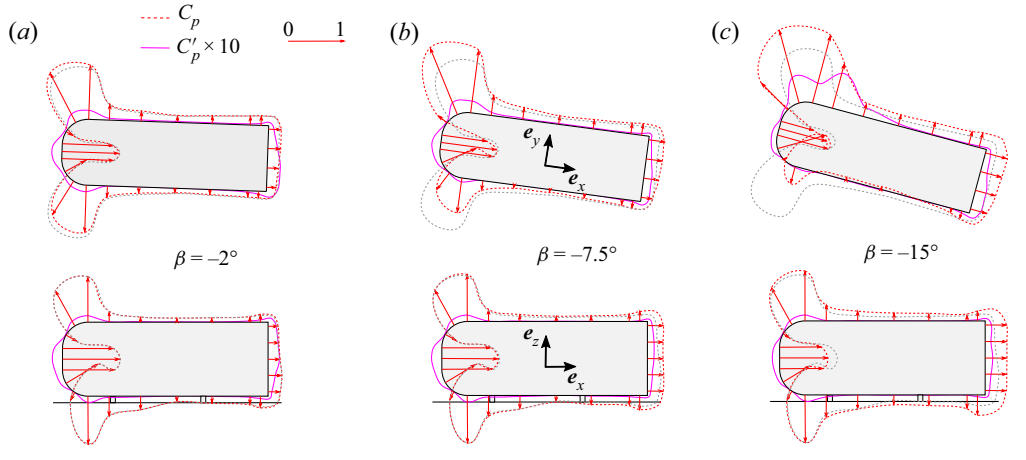

Figure 4. Details as for figure 3 except that the three cases (*a–c*) depict variations with different yaws and no pitch, $\alpha = 0^\circ$, and $C^* = 0.1$.

Yawing the body for a given clearance $C^* = 0.1$ essentially leads to an asymmetry of the pressure distribution in the horizontal section as shown in figure 4 (top row), thus producing the side force. The pressure at the base is also remarkably decreased as the yaw is made continuously larger, indicating a substantial drag increase. At large yaw, the leeward side shows a significant increase in the pressure fluctuations in figure 4(*c*, top), likely to be provoked by a forebody separation. The separation on the leeward side is observable for smaller yaw when the clearance is small, as can be seen in figure 5(*b*, top) for $\beta = -7.5^\circ$ and the smallest achievable clearance $C^* = 0.01$.

The pitch variations increase the asymmetry in the vertical cross-section, as shown in figure 6 (bottom row), which affects directly the lift component. Compared to the equivalent yaw in figure 4(*a*, top), the proximity of the ground clearly amplifies this

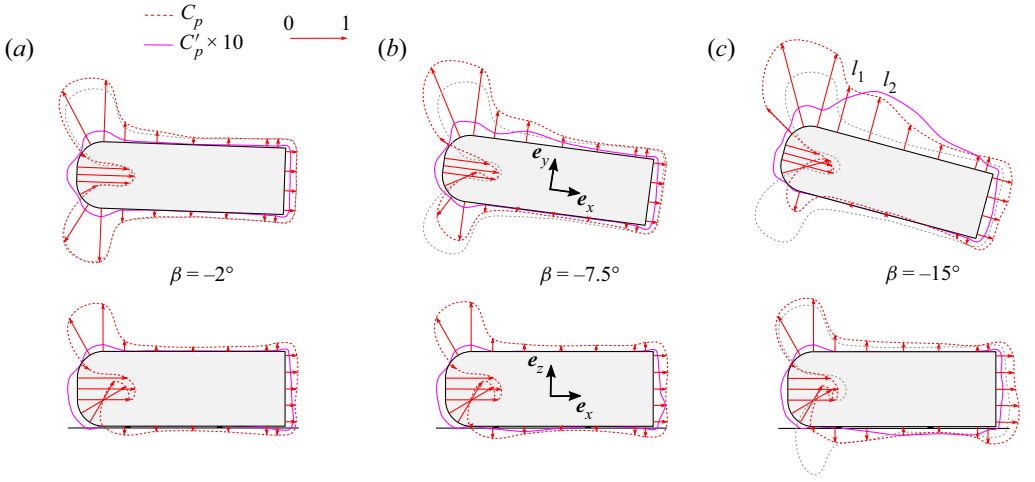

Figure 5. Details as for figure 3 except that the three cases (*a–c*) depict variations with different yaws with no pitch $\alpha = 0°$ and $C^* = 0.01$.

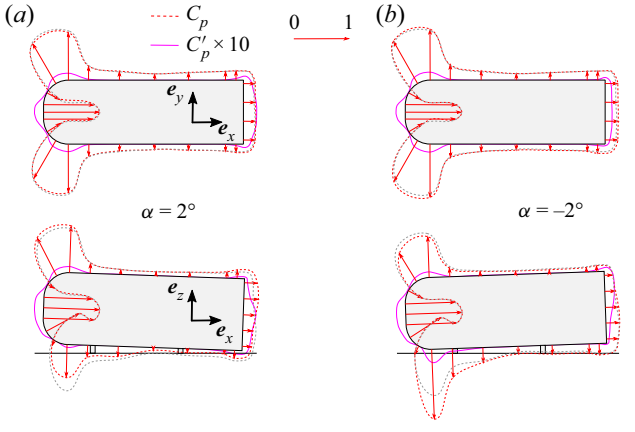

Figure 6. Details as for figure 3 except that the two cases (*a*,*b*) depict variations with different pitches with no yaw, $\beta = 0°$, and $C^* = 0.1$.

asymmetry especially at the nose according to a blockage effect. No noticeable separation compared to the aligned case can be distinguished at the forebody in figure 6 (bottom row) as the pressure fluctuations level remains small. This is due to the small range of pitch investigated.

3.2. *Leeward separation*

The leeward separation on the lateral sides as evidenced in the top rows of figures 4(*c*) and 5(*b*,*c*) are detected for all attitudes using the sum $C'_{pl} = C'_{pl_1} + C'_{pl_2}$ of the pressure fluctuations at the two locations denoted l_1 and l_2 in figure 5(*c*). This criterion indicates the presence of a laminar to turbulent transition of the separated shear, and would be insensitive in the case of a laminar reattachment. For variations of clearance and yaw in figure 7(*a*), large values of C'_{pl} indicate two distinctive regions of body separation in the parametric space: the first region is observed at low clearance $C^* < 0.02$ and large yaw $\beta < -7.5°$, corresponding to cases depicted in figures 5(*b*,*c*); and the second region

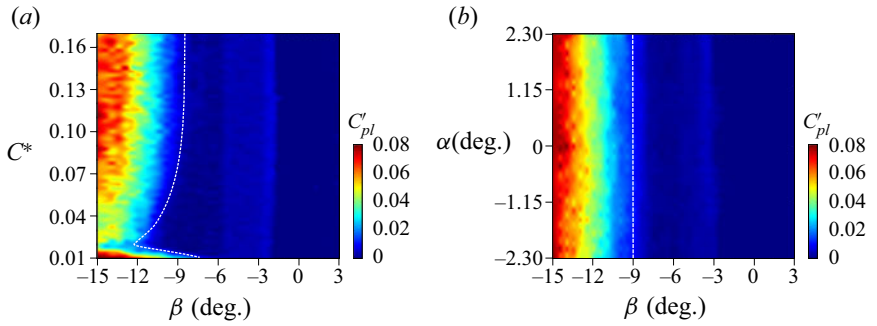

Figure 7. Regions of separation on the lateral leeward side for the variations of (*a*) clearance and yaw $C'_{pl}(\beta, C^*, \alpha = 0^\circ)$, and (*b*) pitch and yaw $C'_{pl}(\beta, \alpha, C^*_0 = 0.1)$.

is observed at larger clearance $C^* > 0.02$ and $\beta < -9^\circ$, corresponding to the case in figure 4(*c*). For variations of pitch and yaw in figure 7(*b*), a single region of leeward separation is seen for $\beta < -9^\circ$, as depicted in figure 4(*c*). The regions of the parameter space for which the leeward side experiences flow separation are delimited by the dashed lines in figure 7. These lines will be superimposed when appropriate onto other results in the following subsections.

3.3. *Wake transitions*

We turn now to the base pressure gradient components as indicators of the wake asymmetry (Grandemange *et al.* 2013*b*). The mean (G_y and G_z) and fluctuating (G'_y and G'_z) components are respectively shown in figures 8 and 9 for both the clearance (panels *a*,*b*) and pitch (panels *c*,*d*) versus yaw mappings. Very clear changes of gradient orientation are observable in figure 8, as well as a large localized crisis of fluctuations in figure 9. It is striking that the gradients fluctuation is orientated exclusively in the vertical direction; i.e. G'_z in figures 9(*b*,*d*) displays the largest fluctuation. This is a strong indication that the wake remains dominated by the z-instability even with yaw and pitch.

We attempted to display these changes by superimposing arbitrarily on the observable transitions the dashed lines on each plot of figure 8, where the red (resp. black) dashed lines are for transitions observed for G_y (resp. G_z). All transition lines are then reported in the recap figures 10(*a*,*b*) that divide the maps into five main regions, labelled I to V. Each region is illustrated in these figures by base pressure distributions for a few configurations of the parametric study displayed as filled black circles. Both regions I in figures 10(*a*,*b*) are obtained from figures 9(*b*,*d*) where large fluctuations are observed. These large fluctuations are due to unsteady dynamics between wake states of opposite vertical gradient components (as shown by $G_y \approx 0$ in figures 8*a*,*c*). The most probable gradient's sign depends on the clearance: it is negative for $C^* < 0.15$ in figure 8(*b*), and positive for $C^* > 0.15$. Pitch-up configurations ($\alpha > 0^\circ$) definitely lock the gradient on a negative value, as can be seen in figure 8(*d*).

In the regions II displayed in figures 10(*a*,*b*), the vertical component of the gradient is positive. This region can be split into three subregions, denoted A, B and C, obtained by combining observations from the mean gradients maps in figure 8: II-A where the gradient is almost vertical, II-B where the gradient is orientated at 45°, and II-C where the vertical component decreases gradually towards zero when entering region III. There is a striking similitude in II subregions between those of the clearance (figure 10*a*) and the

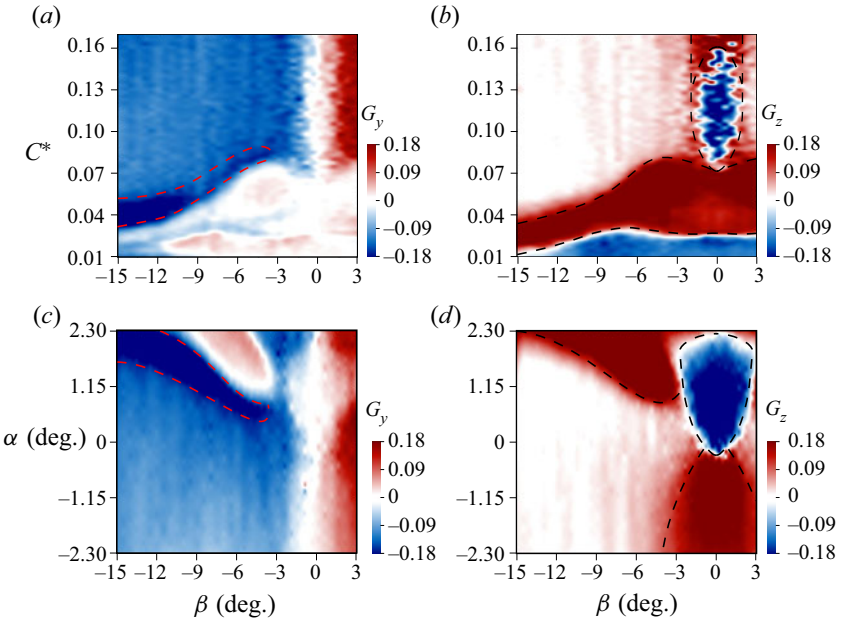

Figure 8. Components of the mean base pressure gradient G_y (*a*,*c*) and G_z (*b*,*d*) for the clearance versus yaw mapping $G_i(\beta, C^*, \alpha = 0^\circ)$ in (*a*,*b*), and the pitch versus yaw mapping $G_i(\beta, C_0^* = 0.1, \alpha)$ in (*c*,*d*). Red (resp. black) dashed lines display noticeable transitions in G_y (resp. G_z).

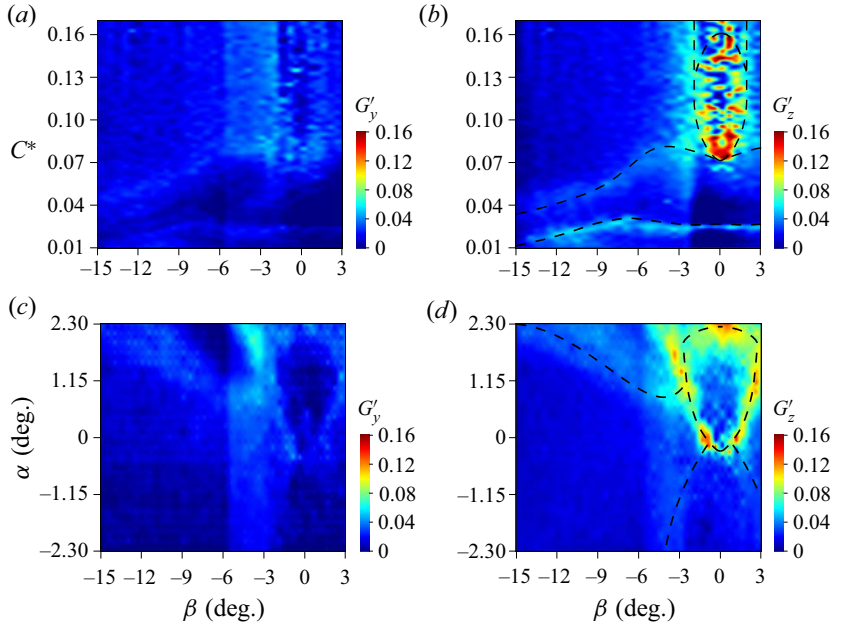

Figure 9. Components of the fluctuating base pressure gradient G'_y (*a*,*c*) and G'_z (*b*,*d*) for the clearance versus yaw mapping $G'_i(\beta, C^*, \alpha = 0^\circ)$ in (*a*,*b*), and the pitch versus yaw mapping $G'_i(\beta, C_0^* = 0.1, \alpha)$ in (*c*,*d*). Dashed lines for G'_z in (*b*,*d*) are the same as for G_z in figures 8(*b*,*d*).

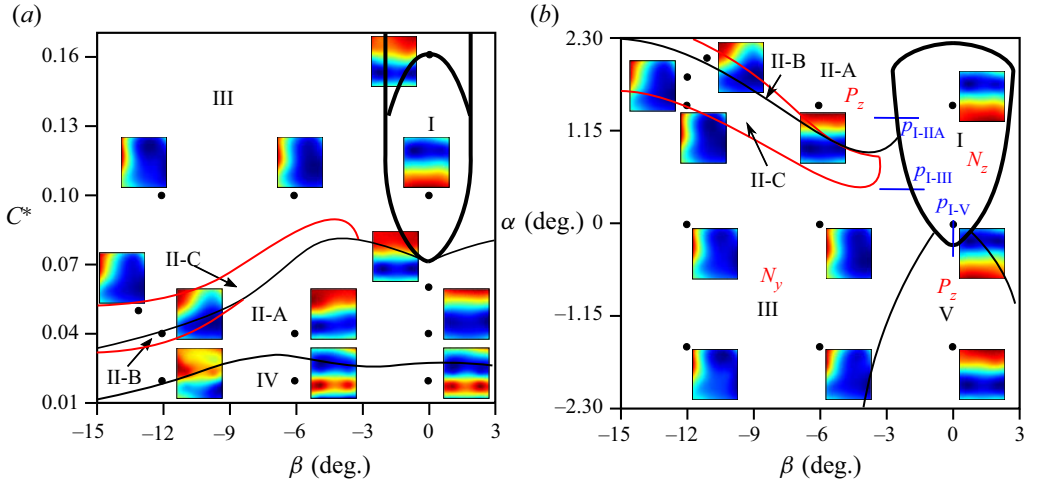

Figure 10. Recap of transitions for (*a*) clearance and (*b*) pitch, versus yaw mappings deduced from figures 8 and 9. All lines are transitions in G_y and G_z reported from figure 8, where red (resp. black) lines are transitions for G_y (resp. G_z). Thick lines depict transitions associated with large base pressure gradient fluctuations. The colour maps show the representative base pressure distribution in different regions, with an autoscale colour bar: red (resp. blue) indicates high (low) pressure. The three blue paths in (*b*) denote the unsteady transitions investigated in § 3.4.

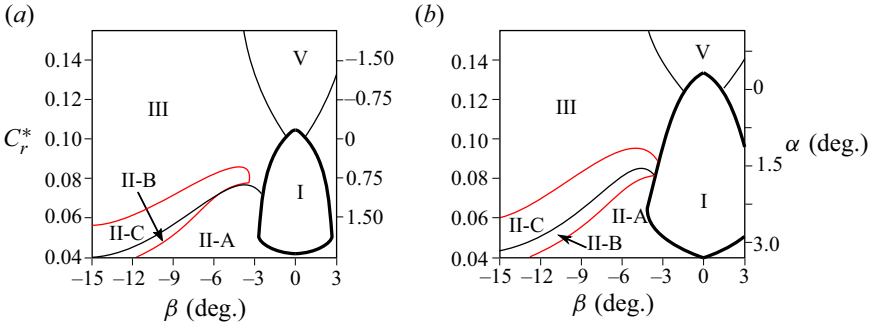

Figure 11. Recap of all transitions for the pitch versus yaw maps represented in the (C_r^*, β) plane with (*a*) $C_0^* = 0.1$ reported from figure 10(*b*), and (*b*) $C_0^* = 0.125$. The pitch α equivalent to C_r^* is displayed as a second axis on the right-hand side of each plot. Same legend for lines as in figure 10.

pitch (figure 10*b*) versus yaw mappings. It points out the important role of the gap between the ground and the lower edge of the base for the base pressure gradient orientation. This gap distance C_r^* as defined in figure 1 is now used to show the transition lines in a (C_r^*, β) plane (figure 11*a*) instead of the (α, β) representation of figure 10(*b*). When comparing figure 11(*a*) to figure 10(*a*) (where $C^* = C_r^*$ as the pitch is zero for these configurations), we find good agreement in the locations of the II subregions with the values of C_r^*. Figure 11(*b*) recaps transitions in the pitch versus yaw map made at a higher clearance, $C^* = 0.125$, than the $C^* = 0.1$ of figure 10(*b*). For this larger clearance, larger pitch angles ($\alpha > 1^\circ$) are necessary to transition in the region II corresponding to the rear gap of $C_r^* \approx 0.1$. As it is slightly larger than the $C_r^* \approx 0.09$ observed in figure 10(*a*), the region II location is also, but at a lower order than the rear clearance, sensitive to the pitch inclination.

Region III gathers configurations with quasi-horizontal gradient, as shown by $G_z \approx 0$ in figures 8(*b*,*d*), with values weakly dependent on the yaw (see figures 8*a*,*c*).

Regions IV in figure 10(*a*) are configurations in absence of flow in the gap C_r^* and correspond to situations depicted in figures 3(*a*) and 5(*a*). The base pressure gradient in region IV is almost vertical everywhere and negative (see figures 8*a*,*b*) because the lower edge of the base is a high-pressure stagnation point due to the back flow of the recirculating bubble. The emergence of the flow in the gap C_r^* when the body is raised evacuates the stagnation point leading to equivalent separations at both the lower and upper edges of the base, but with a positive base pressure gradient. This transition is detailed in (Grandemange *et al.* 2013*a*) for $\beta = 0^\circ$ only, and generalized by the parametric study to the transition line between regions II-A and IV in figure 10(*a*). The transition is accompanied with fluctuations of g_z (see figure 9*b*) and occurs at lower clearance for larger yaw when $\beta < -6^\circ$ (figure 8*b*).

Regions V and I would have been antisymmetric in figure 10(*b*) if the ground and supports were absent. The gradient values in both regions in figures 8(*c*,*d*) almost retrieve this symmetry property. However, only region I is associated with large unsteady dynamics, while region V is clearly not, as shown by the lack of fluctuations for negative pitches in figure 9(*d*). As a result, the positive vertical pressure gradient in region V as depicted in figure 10(*b*) rotates steadily in region III towards a negative horizontal gradient.

For the sake of simplicity, the wake state subjected to the vertical asymmetry is denoted as N_z or P_z with respectively negative ($g_z < 0$ and $g_y \approx 0$) or positive ($g_z > 0$ and $g_y \approx 0$) pressure gradients. Identically, a horizontal asymmetry is denoted as N_y or P_y with respectively negative ($g_y < 0$ and $g_z \approx 0$) or positive ($g_y > 0$ and $g_z \approx 0$) pressure gradients. As reported in figure 10(*b*), region I corresponds to N_z states, regions II-A and V to P_z states, and region III to N_y states. Next, we study the nature of the fluctuation crisis observed when crossing the thick transition lines enclosing region I in figure 10(*b*).

3.4. *Fluctuation crisis of the wake*

From region I in figure 10(*b*), in which the wake presents N_z states, we can see three different possible transitions: towards II-A leading to P_z states, towards III leading to N_y states, and towards V leading also to P_z states. To characterize these unsteady transitions, measurements were repeated along the three paths of attitudes $p_{\text{I-IIA}}$, $p_{\text{I-III}}$ and $p_{\text{I-V}}$ as denoted in figure 10(*b*). They have a better resolution ($\delta\beta = 0.25^\circ$, $\delta\alpha = 0.05^\circ$) as well as a longer recording duration (600s). The evolutions of the probability density functions of the two gradient components g_y and g_z are shown on the left-hand side of figure 12 along each path. On the right-hand side, time series of the vertical gradient component are shown for the most unsteady attitude of the path, marked with a white dashed line.

The wake transitions along $p_{\text{I-IIA}}$ (figure 12*a*) and $p_{\text{I-V}}$ (figure 12*c*) correspond to wake reversals. They have been reported by Bonnavion & Cadot (2018) with a square-back bluff body subjected to the z-instability and also with real car geometries (Bonnavion *et al.* 2019).

The transition along $p_{\text{I-III}}$ has never been reported so far for a z-unstable square-back body. However, it is very similar to the transition observed in pitch for a y-unstable square-back body (Bonnavion & Cadot 2018) or with additional passive disturbances underneath the bluff body (Barros *et al.* 2017). In both cases, the initial horizontal asymmetry transits to a vertical asymmetry.

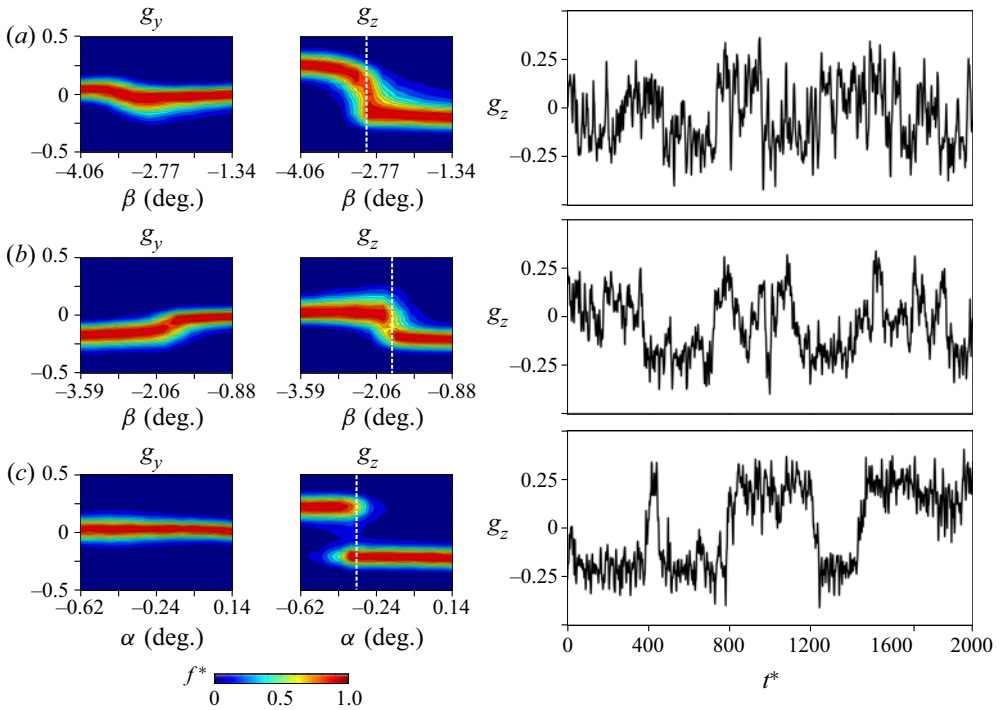

Figure 12. Evolution of the base pressure gradients characteristics along the three paths as displayed in figure 10(*b*): (*a*) $p_{\text{I-IIA}}$: $\alpha = 1.32^\circ$, $C^* = 0.1$; (*b*) $p_{\text{I-III}}$: $\alpha = 0.42^\circ$, $C^* = 0.1$; (*c*) $p_{\text{I-V}}$: $\beta = 0^\circ$, $C^* = 0.1$. Left and middle: normalized probability density functions of the gradient components along the path. Right: time series of vertical pressure gradient g_z for the configuration marked by the white dashed line in the middle figure.

3.5. *Aerodynamic force coefficients*

We turn now to the components of the aerodynamic force coefficients c_x, c_y, c_z that we will respectively call drag, side force and lift coefficients. We recall that c_x is the aerodynamic resistance to the body motion ($V = U_\infty \cos\beta \approx U_\infty$) in the equivalent road condition with crosswind $U_{wind} = U_\infty \sin\beta$. The coefficient c_x is thus related directly to the fuel consumption of the engine.

The variation of the time-averaged drag coefficient C_x in the parametric spaces (β, C^*) and (β, α) is shown in figures 13(*a*) and 14(*a*). This component is split into two contributions, the base drag C_b (figures 13*b* and 14*b*) and all the other contributions $C_x - C_b$ (figures 13*c* and 14*c*), taking into account the total force exerted on the main body and the four cylindrical supports, except the base.

At small clearances $C^* < 0.02$ and large yaws $\beta < -7.5^\circ$ in figure 13(*c*), the increase of contribution $C_x - C_b$ is due to the large leeward separation reported in figure 7(*a*) and depicted in figures 5(*b*,*c*). The quasi-linear variation of $C_x - C_b$ with clearance for all yaw angles is ascribed to the cylindrical supports, for which the projected area is proportional to C^*. It is remarkable that the $C_x - C_b$ contribution decreases towards negative values at large yaw. This thrust must result from the pressure distribution at the forebody as shown in figures 4(*b*,*c*, top) and 5(*b*,*c*, top), similarly to a boat sail propulsion. This propulsion is not observed when the pitch is increased, since large pitches are associated with larger drag contribution in figure 14(*c*). This is because the force balance is not rotating in pitch as it rotates with yaw, i.e. the drag component is always parallel to the ground. To summarize,

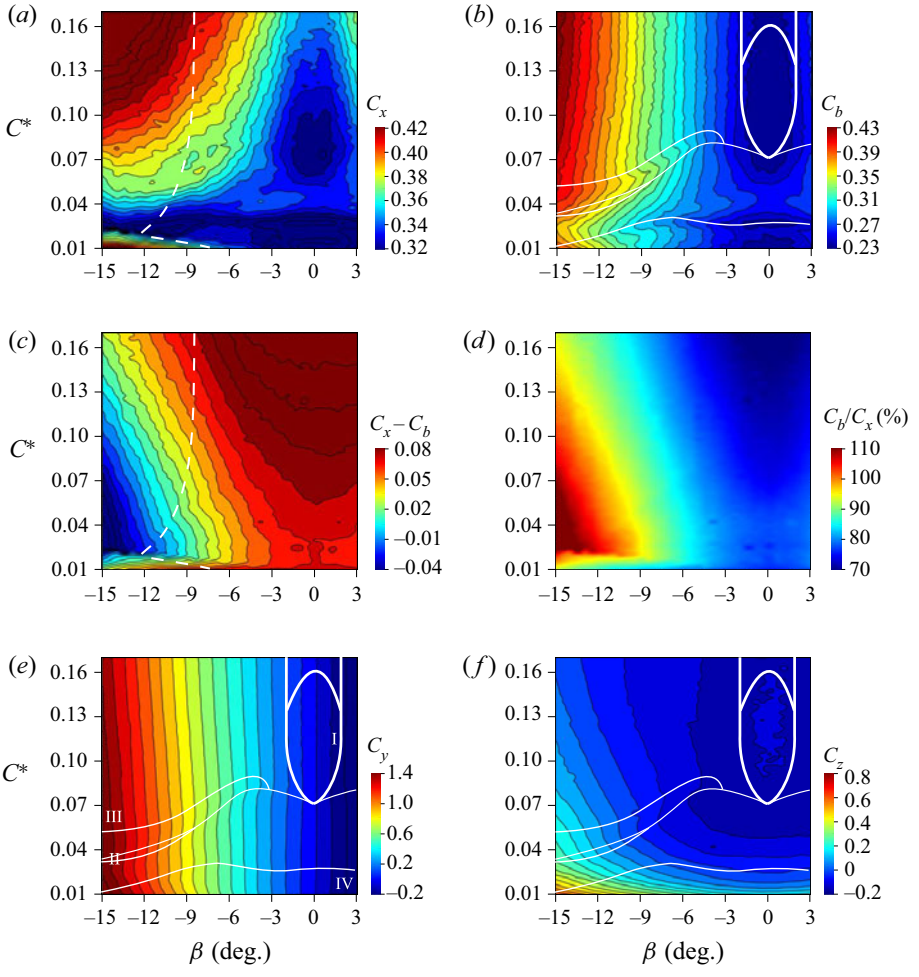

Figure 13. Force coefficient components for the clearance versus yaw mapping (β, C^*, $\alpha_0 = 0^\circ$): (*a*) total drag coefficient C_x; (*b*) base suction C_b; (*c*) remainder drag except for the base suction $C_x - C_b$; (*d*) base suction contribution to the total drag C_b/C_x; (*e*) side force coefficient C_y; (*f*) lift coefficient C_z. Dashed lines in (*a*,*c*) are the leeward separation lines as defined in figure 7(*a*). All lines in (*b*,*e*,*f*) are reported from figure 10(*a*), with thick lines for transitions associated with large base pressure gradient fluctuations. Regions are labelled in (*e*) as defined in figure 10.

crosswind has a beneficial effect on the forebody drag contribution, while pitching the body is always detrimental.

We now focus on the base suction contribution to the total drag C_b/C_x, shown in figures 13(*d*) and 14(*d*). The predominant contribution to the total drag of about 70 % for the aligned condition (similar to the value reported by Ahmed *et al.* 1984) is increased drastically at yaw due to the thrust effect discussed above, and can even increase over 100 % for moderate yaws $\beta < -7^\circ$, depending on the clearance. For small yaw attitudes $|\beta| < 3^\circ$, the main parameter affecting the base suction C_b is either the ground clearance in figure 13(*b*) or the pitch angle in figure 14(*b*). With the increase of the clearance, the base drag C_b undergoes a series of changes, which are consistent with the work of Grandemange *et al.* (2013*a*) for a square-back model with aspect ratio $H/W = 0.74$ at zero yaw. At large

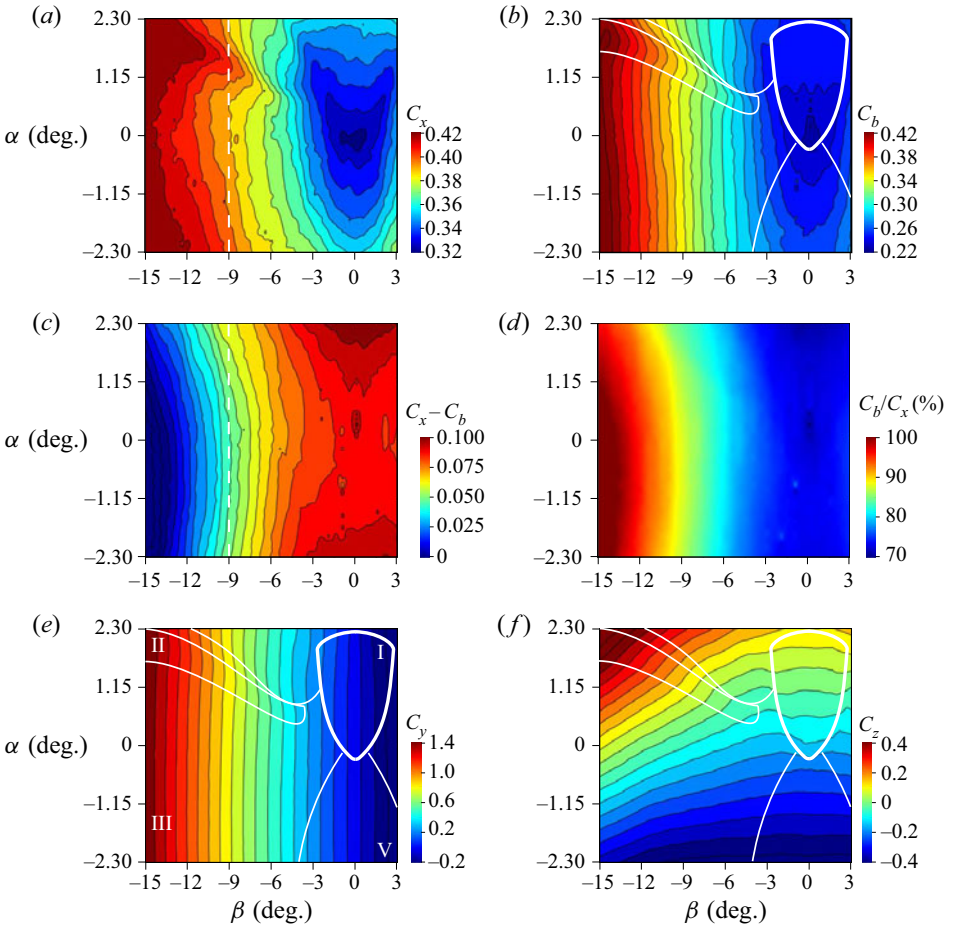

Figure 14. Force coefficient components for the pitch versus yaw mapping (β, $C_0^* = 0.1$, α): (*a*) total drag coefficient C_x; (*b*) base suction C_b; (*c*) remainder drag except for the base suction $C_x - C_b$; (*d*) base suction contribution to the total drag C_b/C_x; (*e*) side force coefficient C_y; (*f*) lift coefficient C_z. Dashed lines in (*a*,*c*) are the leeward separation lines as defined in figure 7(*b*). All lines in (*b*,*e*,*f*) are reported from figure 10(*b*), with thick lines for transitions associated with large base pressure gradient fluctuations. Regions are labelled in (*e*) as defined in figure 10.

clearance ($C^* > 0.07$) corresponding to typical driving conditions on the road, the base drag is independent of the clearance, and presents a linear variation with yaw for $|\beta| > 3^\circ$.

Generally speaking, the lateral force component is obviously related to the body attitude defined by the yaw and the pitch. As shown in figures 13(*e*) and 14(*e*), the side force coefficient C_y is proportional mainly to the yaw angle β, independently on the pitch or the clearance. However, we can see in both figures 13(*e*) and 14(*e*) that the wake asymmetry orientation has an effect on the side force, which will be discussed below. The lift coefficient is found to increase as a quadratic law with the yaw in figures 13(*f*) and 14(*f*). A remarkable correlation with the wake orientation is observable for both parametric studies when comparing the transition lines to the coefficients variation in figures 13(*b*,*e*,*f*) and 14(*b*,*e*,*f*). While base suction C_b is a direct measurement in the wake, the lift C_z and side force C_y coefficients are not, because of the large contribution of the forebody in yaw and pitch as shown in § 3.1. The use of the rear cavity in the next

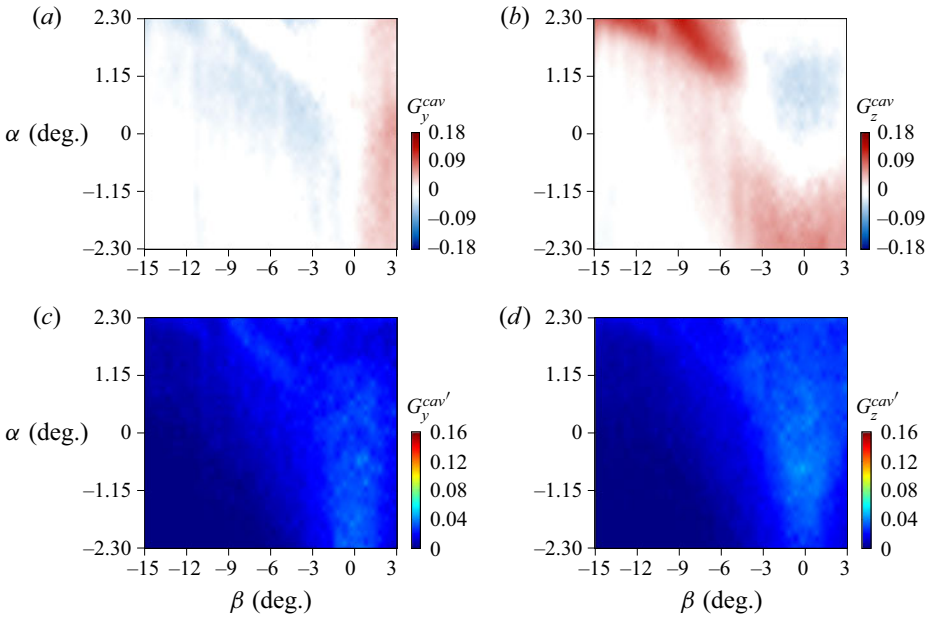

Figure 15. Case with the rear cavity: components of the mean $\boldsymbol{G}(\beta, C_0^* = 0.1, \alpha)$ (a,b) and fluctuating $\boldsymbol{G'}(\beta, C_0^* = 0.1, \alpha)$ (c,d) base pressure gradient for the pitch versus yaw mapping.

subsection enables us to isolate the direct contribution of the wake to both coefficients C_z and C_y as a function of the body attitude.

3.6. *Rear cavity*

We repeated the parametric study for attitudes in yaw and pitch in the space $(\beta, C_0^* = 0.1, \alpha)$ in exactly the same conditions as above but with a rear cavity of depth $d^* = 0.35$ (as depicted in figure 1). Figure 15 shows the mean and fluctuating components of the base gradient $\boldsymbol{g^{cav}}$ measured at the bottom of the rear cavity that should be compared to the flat-back case in figures 8(c,d) and 9(c,d). Except for high positive pitch and large negative yaw in figure 15(b) (corresponding to subregion II-A in figure 10b), the mean gradients are considerably reduced, leading to a uniform base pressure distribution. Transitions between different orientations are still observable but much smoother than those without the cavity, while the unsteady transitions on the region I contour (as defined in figure 10(b) and discussed in § 3.4) have totally disappeared. Instead, a more homogeneous region of low-level fluctuations is observed for both components. The cavity has produced similar effects on the steady instability inhibition, as demonstrated by Evrard *et al.* (2016), where it was attributed to the symmetrization of the recirculation at the base.

Figure 16 shows the pressure gradient $\boldsymbol{j}$ (see (2.5)) measured from the lateral surfaces of the body (T, U, L, R in figure 1), at the closest location to the rear flow separation that is the most influenced by the wake dynamics. We first discuss the flat-back case shown in figures 16(a,c,e,g). Both fluctuating component maps of $\boldsymbol{J'}$ in figures 16(c,g) are very similar to those of $\boldsymbol{G'}$ in figures 9(c,d). As the main source of fluctuations is due to the wake, we should not expect any differences between $\boldsymbol{J'}$ and $\boldsymbol{G'}$. However, their mean values $\boldsymbol{J}$ and $\boldsymbol{G}$ show differences by comparing figures 16(a,e) with figures 8(c,d). They can be explained from the contribution of the flow around the body. The wake transitions

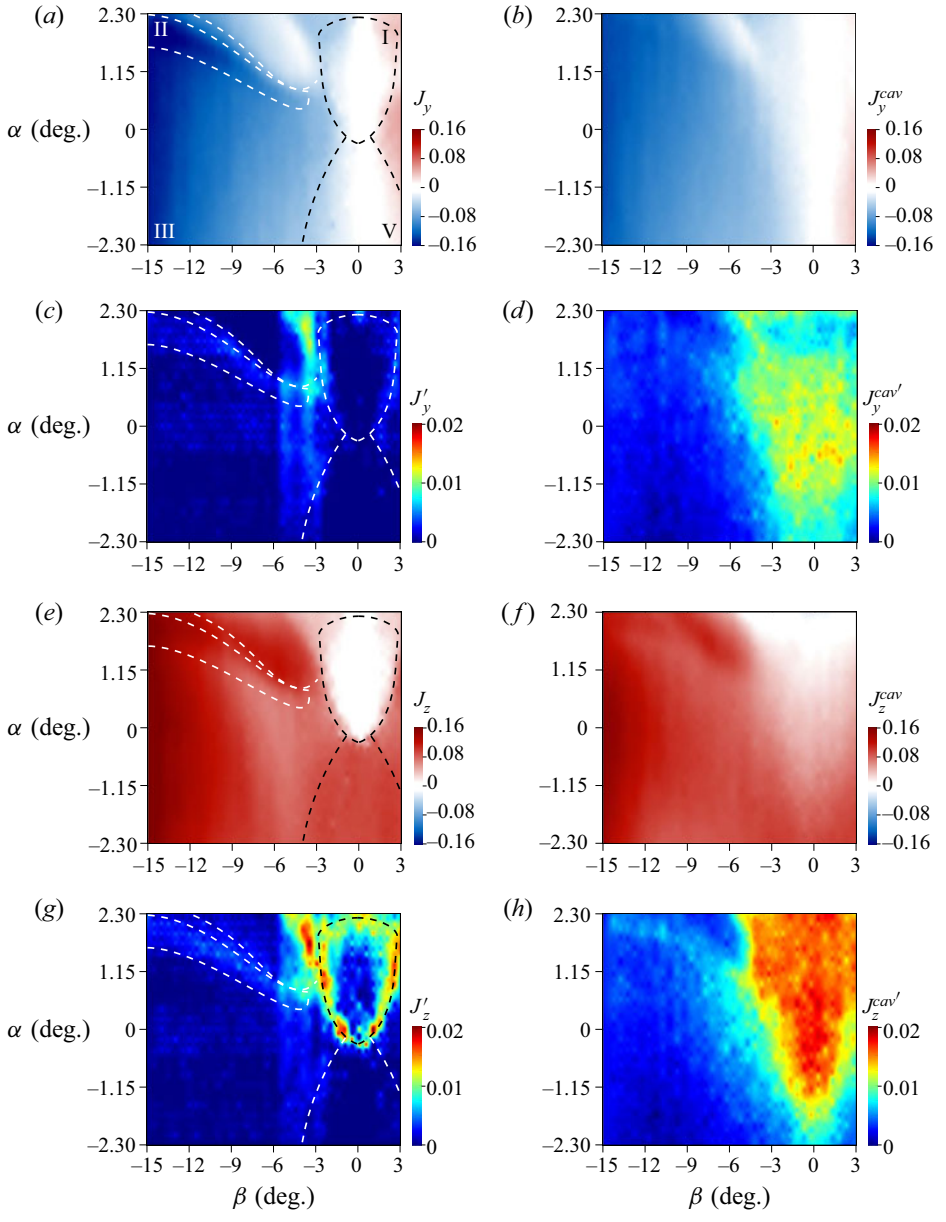

Figure 16. Components of the mean $\boldsymbol{J}(\beta, C_0^* = 0.1, \alpha)$ (*a*,*e*) and fluctuating $\boldsymbol{J'}(\beta, C_0^* = 0.1, \alpha)$ (*c*,*g*) pressure gradient at the rear of the body lateral surfaces. Case with the rear cavity: $\boldsymbol{J^{cav}}(\beta, C_0^* = 0.1, \alpha)$ (*b*,*f*), and $\boldsymbol{J^{cav'}}(\beta, C_0^* = 0.1, \alpha)$ (*d*,*h*). The dashed lines in (*a*,*c*,*e*,*g*) are all transition lines reported from figure 10(*b*), with the regions labelled as in (*a*). Colours are adapted for better contrast.

identified in figure 10(*b*) are still recognizable in figures 16(*a*,*e*), but the absence of changes of sign in $\boldsymbol{J}$ compared to $\boldsymbol{G}$ (J_z is always positive, and J_y keeps the same sign for all negative yaws) is a direct effect of the ground proximity on the flow around the body. Comparing the mean values, $\boldsymbol{J}$ without (figures 16*a*,*e*) and $\boldsymbol{J^{cav}}$ with (figures 16*b*,*f*) the rear cavity, we find similar gradient values because the dominant contribution that is the flow around the body

is the same for both cases. Nevertheless, the smoother variations in figures 16(*b*,*f*) result from the inhibition of the steady instability. On the other hand, it is very striking to observe that the most significant impact of this inhibition is actually displayed by the fluctuation of the gradients in figures 16(*d*,*h*). Their distributions in the maps have changed drastically; instead of having exclusively vertical gradient fluctuations on the contour of region I as in figures 16(*c*,*g*) for the flat-back case, the rear cavity has spread homogeneously the fluctuations in both directions inside regions I and V. As a consequence, the contribution of the wake to the pressure distribution on the lateral surfaces of the body becomes more unsteady when the steady instability is removed by the presence of the cavity, except for attitudes with fluctuation crisis of the wake. This global wake fluctuation with a rear cavity has never been reported, to the authors' knowledge. This interesting result deserves further dedicated investigation of the rear cavity effect that falls out of the scope of this paper. In the following, we study the force coefficients to assess globally the wake effect on the body.

3.7. *Wake contribution to the aerodynamics*

Figure 17 shows the difference of force coefficients $\Delta C_i = C_i - C_i^{cav}$ $(i = x, y, z, yz)$ between the flat-back and the rear cavity body. Since the cavity modifies the flow mainly at the rear of the model, the difference ΔC_i evaluates directly the contribution of the wake on the lateral force coefficients C_y and C_z. The striking resemblance of figures 17(*a*,*b*) to the mean base pressure gradient in figures 8(*c*,*d*) demonstrates clearly the influence of the wake orientation on the pressure loading over the four lateral sides of the body. A negative vertical (resp. horizontal) base pressure gradient produces a positive lift (resp. side force). The extreme contributions of the wake orientation to the lateral force coefficients are ± 0.02. Similar values were obtained by Perry *et al.* (2016) for the Windsor model, Bonnavion & Cadot (2018) for two different aspect ratio Ahmed bodies, and Bonnavion *et al.* (2019) for real cars. Figures 17(*a*,*b*) also evaluate the contribution of the steady wake instability in various crosswind and pitch conditions wherever ΔC_y and ΔC_z are large. It is likely that for large yaw and negative pitch, the flat-back model is no longer subjected to the steady wake instability, which means that the wake asymmetry now results simply from the body attitude. However, there is still a small negative side force change that can be attributed to the flow on the interior lateral side of the cavity that does not exist for the flat-back case. For positive pitch, the instability is still dominant even for large yaw. This is due to the presence of the ground and the associated rear clearance C_r^*, as discussed above.

Eventually, the drag difference in figure 17(*c*) is positive in the whole parametric space, indicating that the cavity always reduces drag. As reported by Evrard *et al.* (2016) and Lucas *et al.* (2017) at $\beta = \alpha = 0^\circ$, the drag reduction mechanism with a cavity is twofold: recirculation elongation and steady instability suppression. The steady instability contribution has been suggested by Grandemange *et al.* (2014) to be a drag induced by the cross-flow force produced by the symmetry breaking. Lorite-Díez *et al.* (2020*a*) showed that the drag difference ΔC_x between the flat-back and the rear cavity base was decreasing monotonically with yaw for a *y*-unstable Ahmed body at zero pitch. We can see in figure 17(*c*) that the *z*-instability produces a new trend due to the transition between the regions I and III, where the drag difference is not monotonic with yaw but reaches a maximum at approximately $\beta \approx -4.5^\circ$. There are actually two main regions where the drag difference ΔC_x is minimal in figure 17(*c*): (i) in region III where the flat-back model

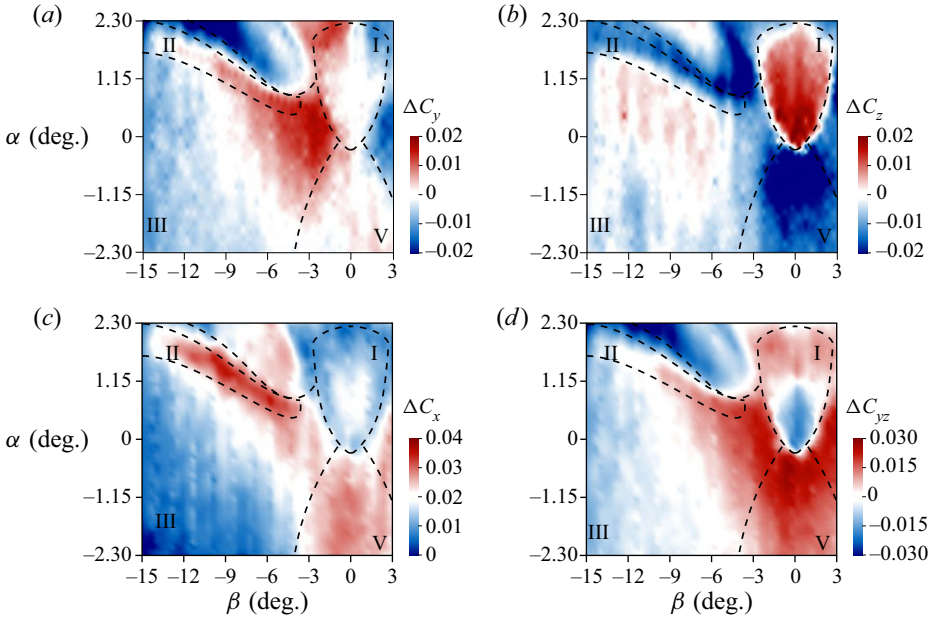

Figure 17. The aerodynamic force difference between the geometry with cavity and without cavity, $\Delta C_i = C_i - C_i^{\mathrm{cav}}$ $(i = x, y, z)$ for pitch versus yaw mapping $(\beta, C_0^* = 0.1, \alpha)$: (*a*) side force coefficient difference; (*b*) lift coefficient difference; (*c*) drag coefficient difference. (*d*) Lift coefficients C_z and C_z^{cav} versus the pitch for attitudes with $\beta = 0^\circ$ and $C_0^* = 0.1$. The dashed lines are all transition lines reported from figure 10(*b*).

is no longer subjected to the steady wake instability, as discussed above; and (ii) in the whole of region I. It can be argued for (i) that in the absence of the steady instability, the drag reduction with the cavity is missing the contribution of the stabilizing effect of the wake, and the only elongation mechanism that remains plausibly explains the low value of drag reduction. For (ii), it is likely that the negative vertical pressure gradient N_z of the z-instability present in region I is responsible for the weak cavity effect on drag.

We now attempt to relate the drag changes and the mean cross-flow force produced by the z-instability with its induced drag effect. For all inclinations of the body investigated ($|\beta| < 15^\circ$), the cross-flow force (perpendicular to the wind axis) and the lateral body force on which the following reasoning is based are quasi-identical. Figure 17(*d*) shows the difference of the mean lateral force coefficient ΔC_{yz} between the flat-back and the rear cavity base, with $C_{yz} = \sqrt{C_y^2 + C_z^2}$. If we assume that the large (resp. small) drag differences in figure 17(*c*) are associated with a large (resp. small) induced drag effect of the mean lateral force due to the z-instability of the flat-back body, then we expect to find a large (resp. small) drag difference in figure 17(*c*) to correspond to increased (resp. decreased) mean lateral force in figure 17(*d*). This correspondence is satisfied only for $\alpha < 1.15^\circ$, where the decreased lateral force in region I in figure 17(*d*) corresponds to the weak drag difference in figure 17(*c*), and the increased lateral force in both regions V and III in figure 17(*d*) correspond to the large drag difference in figure 17(*c*). The simple idea of induced drag modified by the mean additional lateral force of the wake z-instability breaks down at $\alpha > 1.15^\circ$, which corresponds to the sign change of the lift in region I (see figure 14*f*). Unfortunately, for this part, we could not find alternative interpretation with our available data. It probably shows the difficulties of the induced drag

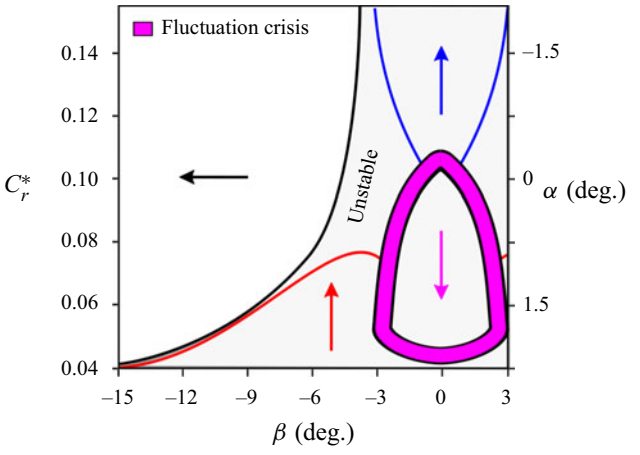

Figure 18. The z-instability domain of the wake as a function of the body attitude (defined by yaw β and pitch α or rear clearance C_r^*) deduced from the rear cavity experiment and transitions in the base pressure gradient. The orientation of the pressure gradient is indicated with arrows.

approach for a complex geometry having more than one surface generating a cross-flow force, such as a wing. Actually, local cross-flow forces over a 3-D body producing globally induced drag with a complex system of longitudinal vortices can compensate to give no net cross-flow force. In that case, there is no net cross-flow to relate the existing induced drag to. A good example is the attitude at $\beta = 0°$, $\alpha = 1.15°$ that has a zero net lateral force (see figure 17*d*),which does not correspond to a minimal base drag configuration (see figure 14*b*). At this attitude, the body inclination that has produced longitudinal vortices at the four sharp longitudinal edges of the body is somehow responsible for substantial additional induced drag.

4. Conclusion

This work explored the sensitivity of the aerodynamics of a flat-back bluff body to its attitude defined by yaw, pitch and ground clearance. The study of the base pressure gradients reveals the presence of sharp transitions, either unsteady or steady, between opposite or right-angle base pressure gradient orientations, leading to the establishment of phase diagrams in the (β, C^*, α_0) and (β, C_0^*, α) parametric spaces. Figure 18 summarizes the phase diagram in the (β, C_0^*, α) space. An equivalent diagram can be retrieved from the other parametric study $(\beta, C^* > 0.04, \alpha_0)$ when plotted with the same rear clearances. The unsteady transitions, comprising the wake bi-stability phenomena, are due to a fluctuation crisis of only the z-component of the base pressure gradient. Their locations have been identified in the attitude spaces as indicated in figure 18.

Experiments are repeated with a rear cavity that inhibits the z-instability in the (β, C_0^*, α) parametric space. Since the flows with and without the rear cavity differ only by their wake influence, the subtraction of their aerodynamics enables the assessment of the wake steady instability contribution to the force. Thus the domain defined from all attitudes featuring a high lateral force difference is assumed to be produced by the steady instability. The obtained domain is displayed in figure 18. While the unstable domain is restricted to small yaw angles $|\beta| < 4°$ for pitch-down attitudes or large rear clearances, it extends to yaw angles up to $|\beta| \approx 15°$ for rear clearances $C_r^* \approx 0.04$. The unstable domain comprises three main regions of a vertically locked base pressure gradient, illustrated

in figure 18. These locked states are surely maintained by a top/down asymmetry of the flow at the base, introduced by any combination of the pitch angle, ground effect and body supports. The questions of why the wake orientates as it does, and why fluctuations crisis occurs only for pitch-up attitudes, require velocity field measurements around the base.

The rear cavity is always found to reduce the drag. Its magnitude is correlated to the regions in figure 18. In particular, the lower effectiveness of the cavity in the region of the negative base pressure gradient indicates that such gradient orientation is favourable for low drag. However, the idea that the z-unstable wake reduces the mean net lateral force on the body, thereby reducing the associated induced drag, fails for all attitudes with large pitch-up values or small rear clearances.

The work focused on the base pressure distribution as a simplified way to investigate thoroughly the sensitivity of the wake to different attitudes. It is clear that the increasing complexity of 3-D separations along the body edges with non-aligned attitudes requires more information, and the nature of their interaction with the steady instability of the wake is an open question.

Finally, the z-instability affects substantially the lateral force and drag for attitudes in the ranges $\pm 5^\circ$ in yaw and $\pm 1^\circ$ in pitch. This fundamental work on a unique geometry then suggests that real cars subjected to the steady instability have increased aerodynamic sensitivity to attitudes within this range. This sensitivity should have clear implications for drag optimization of vehicles when crosswinds are taken into account, but also in the case of mass loading variations modifying the car pitch. In addition, it is especially in the yaw range $\pm 5^\circ$ that Howell (2015) recommends car builders to focus for significant fuel consumption reduction in real driving conditions.

Acknowledgements. The authors would like to acknowledge the invaluable contributions of both the mechanical and electrical workshops of the University of Liverpool to set up the experiment.

Funding. This work has been supported by the Khalifa University of Science and Technology under Award no. CIRA-2019-025. Y.F. wishes to thank the China Scholarship Council (CSC no. 202006260028) for the doctoral financial support.

Declaration of interest. The authors report no conflict of interest.

Author ORCIDs.
Yajun Fan https://orcid.org/0000-0002-6304-1606;
Vladimir Parezanović https://orcid.org/0000-0002-4396-2686;
Olivier Cadot https://orcid.org/0000-0001-7323-6418.

References

Ahmed, S.R., Ramm, G. & Faitin, G. 1984 Some salient features of the time-averaged ground vehicle wake. *SAE Tech. Paper* 840300. Society of Automotive Engineers.

Barros, D., Borée, J., Cadot, O., Spohn, A. & Noack, B.R. 2017 Forcing symmetry exchanges and flow reversals in turbulent wakes. *J. Fluid Mech.* **829**, R1.

Bearman, P.W. 1967 On vortex street wakes. *J. Fluid Mech.* **28** (4), 625–641.

Berger, E., Scholz, D. & Schumm, M. 1990 Coherent vortex structures in the wake of a sphere and a circular disk at rest and under forced vibrations. *J. Fluids Struct.* **4** (3), 231–257.

Bonnavion, G. & Cadot, O. 2018 Unstable wake dynamics of rectangular flat-backed bluff bodies with inclination and ground proximity. *J. Fluid Mech.* **854**, 196–232.

Bonnavion, G., Cadot, O., Évrard, A., Herbert, V., Parpais, S., Vigneron, R. & Délery, J. 2017 On multistabilities of real car's wake. *J. Wind Engng Ind. Aerodyn.* **164**, 22–33.

Bonnavion, G., Cadot, O., Herbert, V., Parpais, S., Vigneron, R. & Délery, J. 2019 Asymmetry and global instability of real minivans' wake. *J. Wind Engng Ind. Aerodyn.* **184**, 77–89.

BRACKSTON, R.D., GARCÍA DE LA CRUZ, J.M., WYNN, A., RIGAS, G. & MORRISON, J.F. 2016 Stochastic modelling and feedback control of bistability in a turbulent bluff body wake. *J. Fluid Mech.* **802**, 726–749.

BURTON, D., WANG, S., SMITH, D.T., SCOTT, H.N., CROUCH, T.N. & THOMPSON, M.C. 2021 The influence of background turbulence on Ahmed-body wake bistability. *J. Fluid Mech.* **926**, R1.

CADOT, O., ALMARZOOQI, M., LEGEAI, A., PAREZANOVIĆ, V. & PASTUR, L. 2020 On three-dimensional bluff body wake symmetry breaking with free-stream turbulence and residual asymmetry. *C. R. Mec* **348** (6–7), 509–517.

CADOT, O., EVRARD, A. & PASTUR, L. 2015 Imperfect supercritical bifurcation in a three-dimensional turbulent wake. *Phys. Rev.* E **91** (6), 063005.

CASTELAIN, T., MICHARD, M., SZMIGIEL, M., CHACATON, D. & JUVÉ, D. 2018 Identification of flow classes in the wake of a simplified truck model depending on the underbody velocity. *J. Wind Engng Ind. Aerodyn.* **175**, 352–363.

DALLA LONGA, L., EVSTAFYEVA, O. & MORGANS, A.S. 2019 Simulations of the bi-modal wake past three-dimensional blunt bluff bodies. *J. Fluid Mech.* **866**, 791–809.

DARGAHI, B. 1989 The turbulent flow field around a circular cylinder. *Exp. Fluids* **8** (1–2), 1–12.

DUELL, E.G. & GEORGE, A.R. 1999 Experimental study of a ground vehicle body unsteady near wake. *SAE Trans.* **108** (6, part 1), 1589–1602.

GARCÍA DE LA CRUZ, J.M., OXLADE, A.R. & MORRISON, J.F. 2017 Passive control of base pressure on an axisymmetric blunt body using a perimetric slit. *Phys. Rev. Fluids* **2** (4), 043905.

EVRARD, A., CADOT, O., HERBERT, V., RICOT, D., VIGNERON, R. & DÉLERY, J. 2016 Fluid force and symmetry breaking modes of a 3D bluff body with a base cavity. *J. Fluids Struct.* **61**, 99–114.

EVRARD, A., CADOT, O., SICOT, C., HERBERT, V., RICOT, D. & VIGNERON, R.I. 2017 Comparative effects of vortex generators on Ahmed's squareback and minivan car models. *Proc. Inst. Mech. Engrs* D*: J. Automobile Engng* **231** (9), 1287–1293.

EVSTAFYEVA, O., MORGANS, A.S. & DALLA LONGA, L. 2017 Simulation and feedback control of the Ahmed body flow exhibiting symmetry breaking behaviour. *J. Fluid Mech.* **817**, R2.

FAN, Y., XIA, C., CHU, S., YANG, Z. & CADOT, O. 2020 Experimental and numerical analysis of the bi-stable turbulent wake of a rectangular flat-backed bluff body. *Phys. Fluids* **32** (10), 105111.

GRANDEMANGE, M., GOHLKE, M. & CADOT, O. 2013*a* Bi-stability in the turbulent wake past parallelepiped bodies with various aspect ratios and wall effects. *Phys. Fluids* **25**, 95–103.

GRANDEMANGE, M., GOHLKE, M. & CADOT, O. 2013*b* Turbulent wake past a three-dimensional blunt body. Part 1. Global modes and bi-stability. *J. Fluid Mech.* **722**, 51–84.

GRANDEMANGE, M., GOHLKE, M. & CADOT, O. 2014 Turbulent wake past a three-dimensional blunt body. Part 2. Experimental sensitivity analysis. *J. Fluid Mech.* **752**, 439–461.

HAFFNER, Y., BORÉE, J., SPOHN, A. & CASTELAIN, T. 2020 Mechanics of bluff body drag reduction during transient near-wake reversals. *J. Fluid Mech.* **894**, A14.

HAFFNER, Y., CASTELAIN, T., BORÉE, J. & SPOHN, A. 2021 Manipulation of three-dimensional asymmetries of a turbulent wake for drag reduction. *J. Fluid Mech.* **912**, A6.

HASSAAN, M., BADLANI, D. & NAZARINIA, M. 2018 On the effect of boat-tails on a simplified heavy vehicle geometry under crosswinds. *J. Wind Engng Ind. Aerodyn.* **183**, 172–186.

HOWELL, J. 2015 Aerodynamic drag of passenger cars at yaw. *SAE Intl J. Passeng. Cars - Mech.* **8** (2015-01-1559), 306–316.

HSU, E.-C., PASTUR, L., CADOT, O. & PAREZANOVIĆ, V. 2021 A fundamental link between steady asymmetry and separation length in the wake of a 3D square-back body. *Exp. Fluids* **62** (5), 95.

HUCHO, W.-H. 1998 *Aerodynamics of Road Vehicles*. SAE International.

HUCHO, W.-H. & SOVRAN, G. 1993 Aerodynamics of road vehicles. *Annu. Rev. Fluid Mech.* **25** (1), 485–537.

KHALIGHI, B., CHEN, K.H. & LACCARINO, G. 2012 Unsteady aerodynamic flow investigation around a simplified squareback road vehicle with drag reduction devices. *J. Fluids Engng* **134** (6), 061101.

LEGEAI, A. & CADOT, O. 2020 On the recirculating flow of three-dimensional asymmetric bluff bodies. *Exp. Fluids* **61** (12), 249.

LI, R., BARROS, D., BORÉE, J., CADOT, O., NOACK, B.R. & CORDIER, L. 2016 Feedback control of bimodal wake dynamics. *Exp. Fluids* **57** (10), 158.

LI, R., BORÉE, J., NOACK, B.R., CORDIER, L. & HARAMBAT, F. 2019 Drag reduction mechanisms of a car model at moderate yaw by bi-frequency forcing. *Phys. Rev. Fluids* **4**, 034604.

LORITE-DIEZ, M., JIMÉNEZ-GONZÁLEZ, J.I., PASTUR, L., CADOT, O. & MARTINEZ-BAZÁN, C. 2020*a* Drag reduction on a three-dimensional blunt body with different rear cavities under cross-wind conditions. *J. Wind Engng Ind. Aerodyn.* **200**, 104145.

LORITE-DÍEZ, M., JIMÉNEZ-GONZÁLEZ, J.I., PASTUR, L., CADOT, O. & MARTÍNEZ-BAZÁN, C. 2020*b* Drag reduction of three-dimensional bodies by base blowing with various gas densities. *Phys. Rev.* E **102** (1), 011101.

LUCAS, J.-M., CADOT, O., HERBERT, V., PARPAIS, S. & DÉLERY, J. 2017 A numerical investigation of the asymmetric wake mode of a squareback Ahmed body – effect of a base cavity. *J. Fluid Mech.* **831** (1), 675–697.

MCARTHUR, D., BURTON, D., THOMPSON, M. & SHERIDAN, J. 2018 An experimental characterisation of the wake of a detailed heavy vehicle in cross-wind. *J. Wind Engng Ind. Aerodyn.* **175**, 364–375.

ÖSTH, J., NOACK, B.R., KRAJNOVIĆ, S., BARROS, D. & BORÉE, J. 2014 On the need for a nonlinear subscale turbulence term in pod models as exemplified for a high-Reynolds-number flow over an Ahmed body. *J. Fluid Mech.* **747**, 518–544.

PASQUETTI, R. & PERES, N. 2015 A penalty model of synthetic micro-jet actuator with application to the control of wake flows. *Comput. Fluids* **114**, 203–217.

PAVIA, G., PASSMORE, M. & SARDU, C. 2018 Evolution of the bi-stable wake of a square-back automotive shape. *Exp. Fluids* **59** (1), 20.

PAVIA, G., PASSMORE, M.A., VARNEY, M. & HODGSON, G. 2020 Salient three-dimensional features of the turbulent wake of a simplified square-back vehicle. *J. Fluid Mech.* **888**, A33.

PERRY, A., PAVIA, G. & PASSMORE, M. 2016 Influence of short rear end tapers on the wake of a simplified square-back vehicle: wake topology and rear drag. *Exp. Fluids* **57** (11), 169.

PODVIN, B., PELLERIN, S., FRAIGNEAU, Y., EVRARD, A. & CADOT, O. 2020 Proper orthogonal decomposition analysis and modelling of the wake deviation behind a squareback Ahmed body. *Phys. Rev. Fluids* **5**, 064612.

ROSHKO, A. 1993 Perspectives on bluff body aerodynamics. *J. Wind Engng Ind. Aerodyn.* **49** (1–3), 79–100.

SCHMIDT, H.-J., WOSZIDLO, R., NAYERI, C.N. & PASCHEREIT, C.O. 2018 The effect of flow control on the wake dynamics of a rectangular bluff body in ground proximity. *Exp. Fluids* **59** (6), 107.

URQUHART, M., VARNEY, M., SEBBEN, S. & PASSMORE, M. 2020 Aerodynamic drag improvements on a square-back vehicle at yaw using a tapered cavity and asymmetric flaps. *Intl J. Heat Fluid Flow* **86**, 108737.

URQUHART, M., VARNEY, M., SEBBEN, S. & PASSMORE, M. 2021 Drag reduction mechanisms on a generic square-back vehicle using an optimised yaw-insensitive base cavity. *Exp. Fluids* **62** (12), 241.

VOLPE, R., DEVINANT, P. & KOURTA, A. 2015 Experimental characterization of the unsteady natural wake of the full-scale square back Ahmed body: flow bi-stability and spectral analysis. *Exp. Fluids* **56** (5), 99.

WORDLEY, S. & SAUNDERS, J. 2008 On-road turbulence. *SAE Intl J. Passeng. Cars – Mech. Syst.* **1**, 341–360.